




Cite this: DOI: 10.1039/d5sc06346a

All publication charges for this article have been paid for by the Royal Society of Chemistry

Cooperative borane activation by tuning hemilability of different Os- κ^2 -N,Se-chelated complexes

Faneesha Assanar, Sourav Gayen, Deepak Kumar Patel, Thalappil Pradeep * and Sundargopal Ghosh *

In an effort to investigate the cooperative activation of boranes, we have designed Os(III) based paramagnetic mono- and bis- κ^2 -1,3-N,Se-chelated complexes, [Os(PPh₃)₂(κ^2 -N,Se-L)Cl₂], **1** and [Os(PPh₃)₂(κ^2 -N,Se-L)(L')], **2–3** (L = C₅H₄NSe; 2: L' = Cl and 3: L' = κ^1 -Se-L). These complexes were synthesised by the thermolysis of [Os(PPh₃)₂Cl₂] with the potassium salt of 2-selenopyridine, which also afforded a diamagnetic species, [Os(PPh₃)₂(κ^2 -N,Se-L)₂], **4**. A comprehensive study utilizing EPR spectroscopy, DFT calculations, and both photochemical and electrochemical analyses has elucidated the distinctive electronic characteristics of these complexes. To probe the electronic influence on hemilability, the OsNCSe osmaheterocycle-based paramagnetic complexes featuring a hard Os(III) centre and a soft Se donor were studied for B–H activation, highlighting synergistic hemilability and metal–ligand cooperativity. Treatment of **2** with [BH₃·SMe₂] yielded the Os(dihydridoborate)(octatrihydridoborate) complex, [Os(PPh₃)₂(κ^3 -H,H,N-BH₃L)(κ^2 -H,Se-B₃H₇L)] (**5**) via ring opening of both Os–Se and Os–N bonds and the Os–borallyl complex, [(PPh₃)(H)₂Os(η^5 -B₃H₅L₂)] (**6**) through cleavage of the Os–N bonds. To further assess steric effects on cooperative borane activation, **2** was treated with the bulky aryl-substituted borane BH₂R (R = (CF₃)₂C₆H₃), which afforded [(PPh₃)Os(κ^3 -H,Se,Se'-(NHRBSeBHRN)(SeC₅H₄)₂)] (**7**) via dual Os–N bond cleavage and insertion of two BHR units followed by B–Se bond formation. Interestingly, we have isolated a unique vertex-fused metallaborane cluster, **8** from the reaction of **6** with an excess of borane. In stark contrast, the diamagnetic bis- κ^2 -1,3-N,Se-chelated complex [Os(PPh₃)₂(κ^2 -N,Se-L)₂], **4** exhibited no tendency to activate sterically demanding boranes. However, using an electronically distinct ligand framework in [Os(PPh₃)₂(κ^2 -N,S-C₇H₄NS₂)₂] (**4^{mbz}**), we observed notable B–H activation patterns of BHR₂ that led to the isolation of the Os(σ -borate) complex, [Os(PPh₃)₂(κ^2 -N,S-C₇H₄NS₂)(κ^3 -H,S,S'-HBR₂(C₇H₄NS₂))] (**11**), where the steric hindrance from the aryl substituents prevented dual-site activation. The bonding insights of these activated species were investigated on the basis of DFT calculations.

Received 19th August 2025
Accepted 26th November 2025

DOI: 10.1039/d5sc06346a

rsc.li/chemical-science

Introduction

Metal–ligand cooperativity (MLC) has experienced immense growth over the past few decades as a powerful mechanistic strategy in the field of bond activation and catalysis. It serves as an alternative to conventional catalysis due to the synergistic interaction between the metal and ligand, which plays a crucial role in facilitating both bond breaking and bond formation processes.^{1–3} In particular, MLC has been widely investigated in the activation of various E–H (E = H, B, C, N, O or Si) bonds^{4–10} and has subsequently been employed in a range of catalytic reactions.^{11–13} In the context of MLC, several strategies have been developed to promote the E–H bond activation process: (a) utilizing a combination of a Lewis acidic metal and a Lewis

basic ligand that cooperatively cleave the E–H bond in a synergistic fashion;^{4,5} (b) employing the inverse arrangement, where Lewis acidic ligands abstract electrons from the donor site of the substrate, with the metal acting as a Lewis base to cooperatively facilitate bond activation;^{6,7} (c) using complexes containing aromatic chelating ligand frameworks, which can undergo dearomatization through deprotonation to provide a reactive site for cooperative bond activation;^{8,9} (d) incorporating redox non-innocent ligands¹⁰ that either directly mediate the bond activation process or act as electron reservoirs within the catalytic cycle.

In the context of type (a), the predominant class of Lewis basic ligands are typically found in a multidentate framework. Notably, metal complexes featuring hemilabile 1,3-chelating homo and hetero bidentate ligands have garnered significant interest in small molecule activation, as a key attribute of these ligands is their ability to provide coordinative unsaturation at

Department of Chemistry, Indian Institute of Technology Madras, Chennai 600036, India. E-mail: sghosh@iitm.ac.in; pradeep@iitm.ac.in



the metal centre. For instance, Yamaguchi proposed an Ir(III) complex (**I**),¹⁴ featuring a κ^2 -*N,O*-pyridionate ligand as an intermediate species in the oxidant-free catalytic oxidation of alcohols.^{14a} Subsequently, Rauchfuss demonstrated that complex **I** functioned as a more efficient catalyst in the same context.^{14b} Schafer and Love developed group-9 phosphoramidate complexes with different ancillary ligands (**II** and **III**, Chart 1), which promote B–H and C–H activation processes.¹⁵ These complexes were subsequently utilized in catalytic chemoselective hydroboration of aldehydes and anti-Markovnikov *O*-phosphoramidation of alkynes. Interestingly, a proton responsive bifunctional ruthenium complex, **IV** promoted the facile E–H bond activation in H₂ and HBPIn across the Ru–O bond.¹⁶ Beyond traditional hemilabile ligands, Gessner and co-workers designed a ruthenium-based 1,3-chelated complex (**V**) with a carbene ligating centre, where substrate activation induces a transition between a carbene and an alkyl ligand without complete cleavage of the M=C bond.^{5a}

In the course of our recent studies, we have synthesized a group of early- and late-transition metal-based mono- and bis- κ^2 -1,3-*N,S*-chelated complexes and investigated their role in the cooperative activation of E–H (E = B, C or Si) bonds in small molecules.^{17–19} The hemilability of four-membered metallaheterocycles, arising from the coexistence of hard (N) and soft (S) donor sites within polydentate ligands, was pivotal in facilitating E–H bond activation. For instance, we have developed Ru- and Os-based bis- κ^2 -1,3-*N,S*-chelated species featuring non-innocent ligands (**VI**, Chart 1), which upon activation of the simplest borane, [BH₃·SMe₂], resulted in the formation of unique σ -borate complexes.^{17b,c} However, in the field of MLC, the influence of concerted modulation of electronic properties in both metal and ligand scaffolds remains uncharted. In pursuit of this objective, we have designed different osmaheterocycles by fine-tuning the hardness of both the metal and ligand components. In this study, we synthesised a series of κ^2 -*N,Se*-chelated Os(III) complexes such as [Os(PPh₃)₂(κ^2 -*N,Se*-C₅H₄NSe)Cl₂] (**1**), [Os(PPh₃)₃(κ^2 -*N,Se*-C₅H₄NSe)₂Cl] (**2**) and [Os(PPh₃)₃(κ^2 -*N,Se*-C₅H₄NSe)₂(κ^1 -*Se*-C₅H₄NSe)] (**3**), and engaged them in the cooperative activation of boranes. The perturbed hemilability of the OsNCSe heterocycle led to the cleavage of the

Os–N and Os–Se bonds, which facilitated the cooperative activation of free borane. Furthermore, a comparative study was conducted to evaluate the impact of steric and electronic factors by employing both substituted and unsubstituted hydroborane reagents in the cooperative activation process. The activation of sterically encumbered boranes enabled the successful isolation of unique Os-(σ -borate) complexes, utilizing a series of both paramagnetic and diamagnetic Os-*N,E*-chelated complexes (E = S or Se).

Results and discussion

Recently, we successfully synthesised Cp* based κ^2 -*N,Se*-chelated group-6 complexes from the reaction of [Cp**M*(CO)₃Cl] (M = Mo, W) and [K⁺L[−]] (L = C₅H₄NSe).¹⁹ With the objective of synthesizing chelated osmium complexes containing a heavier chalcogen atom, we performed the thermolysis of [Os(PPh₃)₃Cl₂], with excess [KL] at 60 °C. The reaction yielded complexes **1**, **2**, **3** and **4** which were further isolated in their purest forms by chromatographic techniques (Scheme 1). The complexes were characterized by different spectroscopic methods, mass spectrometry and X-ray diffraction studies. The ¹H NMR spectra for complexes **1**, **2**, and **3** showed several broad resonance peaks in the upfield region, while the ³¹P{¹H} NMR spectra did not reveal any noteworthy signals. In contrast, the ¹H NMR spectrum of **4** displayed aromatic signals within the chemical shift range of δ = 8.00–6.25 ppm. Furthermore, species **4** exhibited a single resonance peak at δ = −6.3 ppm in the ³¹P{¹H} NMR spectrum. This detailed analysis suggested that complexes **1**, **2**, and **3** exhibit paramagnetic behavior, whereas complex **4** appears to be diamagnetic in nature. Mass spectrometric analysis of **1**, **2**, **3**, and **4** indicated that their respective molecular formulae are [Os(PPh₃)₂(L)Cl₂], [Os(PPh₃)(L)₂Cl], [Os(PPh₃)(L)₃], and [Os(PPh₃)₂(L)₂]. However, a clear assignment could not be done until the single-crystal X-ray diffraction analysis of these species was carried out.

As illustrated in Fig. 1 (left), the molecular structure of complex **1** can be classified as a mono- κ^2 -*N,Se*-chelated complex of Os(III), represented as [Os(PPh₃)₂(κ^2 -*N,Se*-L)Cl₂]. The molecule exhibited approximately C_s symmetry, with the σ -plane containing the bidentate ligand and two chlorine atoms. On the other hand, the solid-state structure of complex **2** was identified as a bis- κ^2 -*N,Se*-chelated Os(III) complex, where the osmium centre is coordinated to two bidentate selenopyridinyl ligands, one chloride, and one PPh₃ ligand (Fig. 1, middle). The Os–Cl bond lengths and the bite angles of the osmaheterocycles in complexes **1** and **2** are comparable. The mono- κ^2 -*N,Se*-chelated complex **1** was formed through the release of one PPh₃ ligand from [Os(PPh₃)₃Cl₂], followed by the coordination of a selenopyridinyl ligand (Scheme 1). The subsequent dissociation of another PPh₃ ligand from complex **1** and the binding of an additional unit of ligand (L) with concomitant elimination of KCl afforded complex **2**. Although we were unable to obtain any suitable crystals for the XRD analysis of **3**, it can be identified as [Os(PPh₃)₃(κ^2 -*N,Se*-L)₂(κ^1 -*Se*-L)] based on mass spectrometry and preliminary spectroscopic data.^{17c} The primary distinction between complexes **2** and **3** stems from the substitution of the

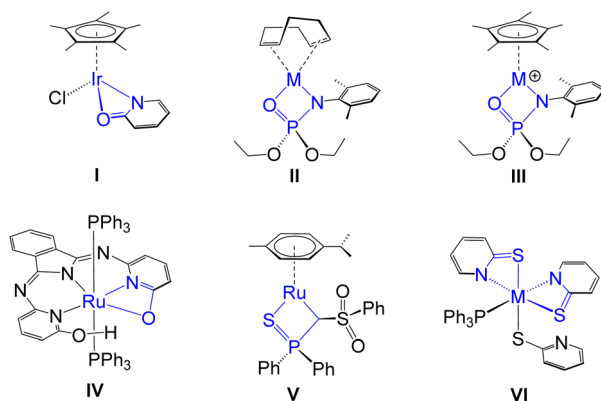
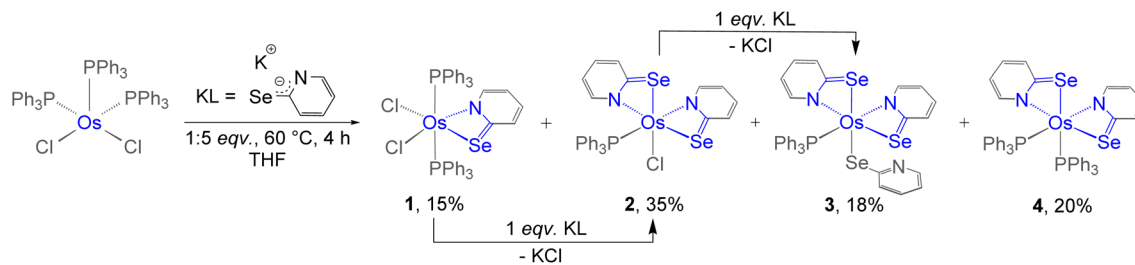


Chart 1 Various TM complexes featuring 1,3-chelated hemilabile ligands (M = Rh and Ir for **II** and **III**; M = Ru and Os for **VI**).





Scheme 1 Syntheses of Os(II) and Os(III)-N,Se-chelated complexes, 1–4.

chloride ligand with a non-innocent ligand. The formation of complex 3 can be rationalized by the monodentate coordination of the selenopyridinyl ligand subsequent to the elimination of KCl. The X-ray diffraction analysis of a suitable orange crystal of complex 4 revealed an octahedral geometry around the Os centre, which includes two κ^2 -1,3-N,Se-chelated rings and two triphenylphosphine ligands (Fig. 1, right). This complex was formed by the dissociation of one PPh₃ ligand from [Os(PPh₃)₃Cl₂], followed by coordination of two selenopyridinyl ligands with concurrent KCl elimination.

To verify the monophasic nature of complexes 1 and 2, powder X-ray diffraction (PXRD) patterns were compared with those simulated from their single-crystal X-ray diffraction (SCXRD) data. The powder XRD patterns of both complexes showed reasonable agreement with the simulated patterns based on their single-crystal structures, confirming the homogeneity of the bulk samples (Fig. S6 and S9). However, a few unidentified low-intensity reflections were observed in both cases, which do not significantly affect the overall bulk phase purity. These results support that the synthesized complexes are largely monophasic and homogeneous.

The paramagnetic properties of complexes 1, 2 and 3 were examined using electron paramagnetic resonance (EPR) spectroscopy at both room temperature and low temperature. While

the room temperature EPR spectra of these species in CH₂Cl₂ (1 and 2) and toluene (3) solution were inconclusive, the X-band frozen glass EPR spectra provided valuable insights. As shown in Fig. 2(a) and (c), the EPR spectra of complexes 1 and 2 exhibited a rhombic pattern with three distinct g values. For both complexes, the g_z values (1: 2.724; 2: 2.851) and g_y values (1: 2.227; 2: 2.052) were clearly resolved, whereas the g_x signal appeared broadened and was observed over a range of 1.2–1.7. The line broadening and reduced spectral resolution of these EPR signals are attributed to the pronounced spin–orbit coupling observed in heavy transition metals such as osmium. Furthermore, density functional theory (DFT) calculations revealed that the Mulliken spin density of the unpaired electron in 1 and 2 is predominantly localized on the Os atom (1: +0.87; 2: +0.71) (Fig. 2(b) and (d)). Notably, a substantial spin density was also detected on the Cl atom in 2, which suggests that coupling with the chloride ligand may have contributed to the observed broadening of the EPR signal. To complement these findings, an Evans NMR study was carried out to determine the solution-state magnetic susceptibility. The experimentally determined magnetic moments (μ_{exp}) of 1 (1.68 μ_B) and 2 (1.80 μ_B) are in good agreement with the theoretically expected value (1.73 μ_B). This indicated that both complexes exhibit a low-spin Os(III) (5d⁵) electronic configuration, consistent with previously

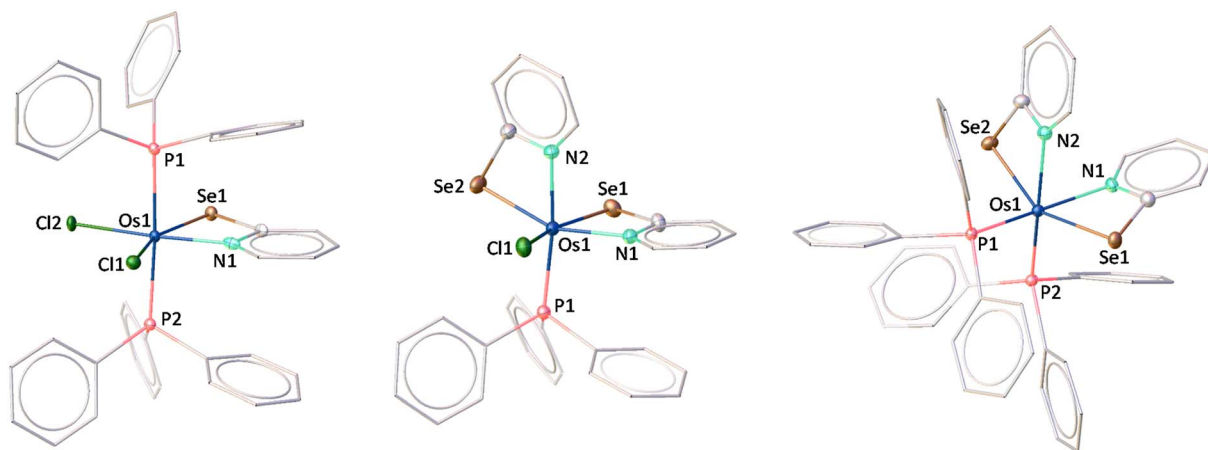


Fig. 1 Molecular structure and labelling diagram of 1 (left), 2 (middle) and 4 (right). Selected bond lengths (Å) and bond angles (°) of 1: Os1–N1 2.093(4), Os1–Se1 2.5518(6), Os1–Cl1 2.3672(13), Os1–Cl2 2.3840(13), Se1–Os1–N1 68.31(13); 2: Os1–N1 2.110(3), Os1–N2 2.098(2), Os1–Se1 2.4510(3), Os1–Se2 2.5351(4), Os1–Cl1 2.3676(8), Se1–Os1–N1 70.16(7), Se2–Os1–N2 68.56(7); 4: Os1–N1 2.154(8), Os1–Se1 2.5494(11), Se1–Os1–N1 68.3(2), and Se2–Os1–N2 68.1(2) (aromatic hydrogens are not shown for better clarity).



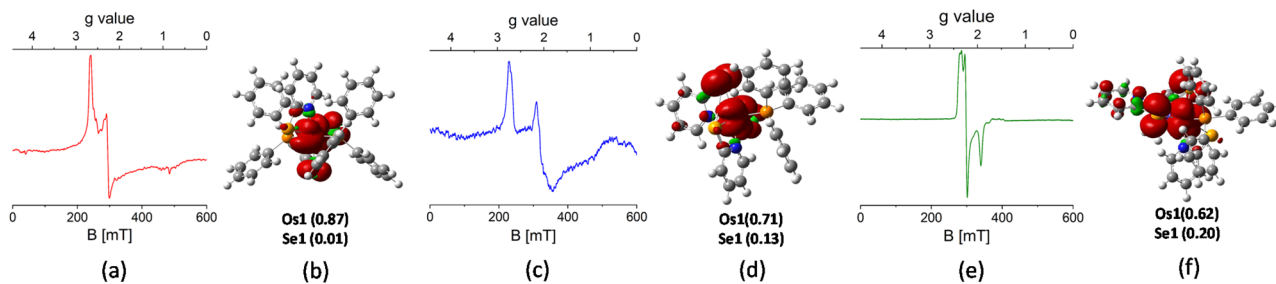


Fig. 2 EPR spectra of **1** (a), **2** (c) and **3** (e); spin density plots of **1** (b), **2** (d) and **3** (f).

reported Os(III) systems.²⁰ Furthermore, the EPR spectrum of **3** exhibited a rhombic pattern with a relatively lower g_z value (2.324) compared to **1** and **2** (Fig. 2(e)). In this context, spin density analysis revealed a significant accumulation of spin density on the Se atom of κ^2 -Se-L, accompanied by a decrease in spin density on the metal atom (Fig. 2(f)). Thus, complex **3** can be described as a superposition of two resonating forms: $[(L^-)Os^{III}]$ and $[(L^+)Os^{II}]$, similar to $[M(PPh_3)(\kappa^2-N,S-C_5H_4NS)_2(\kappa^1-S-C_5H_4NS)]$ ($M = Ru, Os$).^{17b,c} Due to the pronounced spin-orbit coupling in predominantly metal-centred spin systems like **1** and **2**, a higher degree of anisotropy was observed in comparison to **3**.

Owing to the distinct ligand environments around the Os(III) centre in these paramagnetic complexes, we were interested in exploring their redox properties. Redox potentials were measured by cyclic voltammetry, with all values referenced to the Fc^+/Fc couple, as summarized in Table S1. The cyclic voltammograms of complexes **1** and **2** revealed two quasi-reversible redox processes each (**1**: $E_{1/2} = -0.727$ V and 0.737 V; **2**: $E_{1/2} = -0.850$ V and 0.621 V), well-separated within the electrochemical window (Fig. 3(a) and (b)). The cathodic and anodic waves are attributed to the Os^{III}/Os^{II} reduction and Os^{III}/Os^{IV} oxidation processes, respectively. Similar redox behaviour and assignments have been reported for other Os(III) complexes.^{21,22} Furthermore, the cyclic voltammogram of complex **3** yielded three quasi-reversible redox processes where signals at $E_{1/2} = -0.948$ V and 1.123 V correspond to the Os^{III}/Os^{II} and Os^{IV}/Os^{III} couples, respectively (Table S1). In addition to this, another quasi-reversible wave at 0.148 V is associated with a redox event centred on the dangling heterocyclic ligand, assigned to the $Os^{II}(L^+)/Os^{III}(L^-)$ redox couple. This behaviour

closely resembles that observed in redox non-innocent ligand-based Ru and Os complexes, $[M(PPh_3)(\kappa^2-N,S-L')_2(\kappa^1-S-L')]$ ($M = Ru, Os$; $L' = C_5H_4NS, C_7H_4NS_2$) which was recently reported by our group.^{17b,c} Furthermore, the cyclic voltammogram of the diamagnetic κ^2 -N,Se chelated complex, **4** exhibited characteristic redox events associated with the Os^{III}/Os^{II} and Os^{IV}/Os^{III} couples, which is consistent with the electrochemical behaviour observed for its sulfur analogue.^{17c}

With an objective to gain more insightful information about the electronic transitions and structural characteristics of these Os-N,Se chelated complexes, UV-vis absorption spectroscopy was performed on complexes **1**, **2**, **3** and **4** in CH_2Cl_2 . All these complexes exhibited intense absorption in the UV region and a notably distinct absorption pattern in the visible region. The strong absorption in the high-energy region appeared due to the $\pi-\pi^*$ transitions in ligand moieties. In addition, relatively weaker bands observed in the 300–400 nm range for both Os(II) and Os(III) species were ascribed to ligand-to-metal charge transfer (LMCT) transitions (Fig. 3(d) and S15). Notably, the paramagnetic Os(III)-N,Se chelated complexes exhibited broad absorptions extending into the lower-energy visible region, which can be assigned to the $d(Os^{III}) \rightarrow \pi^*(\text{ligand})$ metal-to-ligand charge transfer (MLCT). The introduction of an additional κ^2 -N,Se-L ligand in complex **2** caused a hypsochromic shift of this peak compared to complex **1**. Furthermore, a bathochromic shift in the lower-energy absorption band was observed when going from complex **2** to **3**, attributed to the presence of a different monodentate anionic ligand. Time-dependent DFT (TD-DFT) analysis shows that the transitions calculated at longer wavelengths for these complexes correspond to specific electronic excitations (Table S2). In complex **3**,

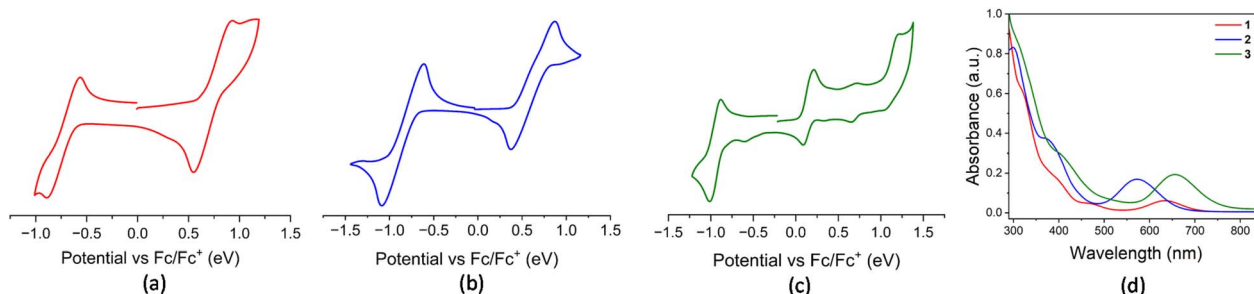


Fig. 3 Cyclic voltammograms of **1** (a), **2** (b) and **3** (c) collected at 100 $mV s^{-1}$; (d) combined UV-vis spectra of **1**, **2** and **3**.



the transition at longer wavelength mainly arises from the excitations from β -HOMO-1 to β -LUMO, while in complex **2**, analogous transitions from β -HOMO-2 and β -HOMO-3 to β -LUMO are observed in a relatively higher energy region.

It is worth noting that **2** can be regarded as electronically analogous to the $[(L^-)Os^{III}]$ tautomer of VI^{Os} (*vide supra*, Chart 1) **17c** due to the absence of a non-innocent ligand. As a result, the osmium centre in **2** exhibits enhanced hardness associated with its higher oxidation state, while the sulfur atom in the osma-heterocycle of VI^{Os} is replaced by a relatively softer selenium atom in **2**. To examine the hemilability of the OsNCSe heterocycle in **2**, its reactivity with free borane was investigated under various conditions. Thermolysis of **2** with four equivalents of $[BH_3 \cdot SME_2]$ at 60 °C changed its colour from deep green to orange and yielded **5** and **6** along with some air and moisture sensitive products (Scheme 2). The $^{31}P\{^1H\}$ NMR spectrum of **5** displayed a singlet at $\delta = 27.9$ ppm which suggested the retention of the PPh_3 unit. The appearance of four chemical shifts at $\delta = 59.9, 14.2, 4.6$ and -15.2 ppm in the $^{11}B\{^1H\}$ NMR spectrum was attributed to the presence of four different boron environments. In addition to the aromatic region peaks, the room temperature 1H NMR spectrum of **5** unveiled three types of broad signals at $\delta = -11.66, -11.61$ and -7.65 ppm in the upfield region. Additionally, mass spectrometry revealed isotopic distribution patterns at m/z 818.0868, consistent with the molecular formula $[C_{28}H_{31}PN_2Se_2B_4Os]$. However, a comprehensive understanding could not be achieved until single-crystal X-ray diffraction analysis of complex **5** was performed.

The X-ray diffraction study of **5** was carried out on an orange crystal obtained from the slow evaporation of hexane layered CH_2Cl_2 solution. As illustrated in Fig. 4, the osmium centre is coordinated to a substituted octatrihydridoborate unit, B_3H_7L , where its interaction with the metal fragment appears to differ from that observed in conventional TM-octatrihydridoborate complexes.^{23,24} Interestingly, the B2 atom is coordinated to osmium through an Os-H-B interaction, while a selenopyridinyl group bridges between Os1 and B1. The Os1-B1 bond length is shorter than that of Os1-B2, likely due to a secondary interaction mediated by the selenopyridinyl unit. In this context, the broad shielded 1H chemical shifts at $\delta = -7.65$ ppm can be attributed to the presence of the Os-H-B unit. However, a definitive upfield signal characteristic of a B-H-B unit was not observed in the room-temperature 1H NMR spectrum. To probe this further, variable-temperature (VT) 1H NMR studies were performed. Upon lowering the temperature, two broad upfield

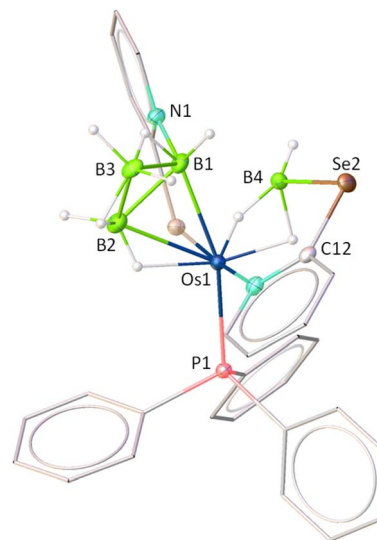
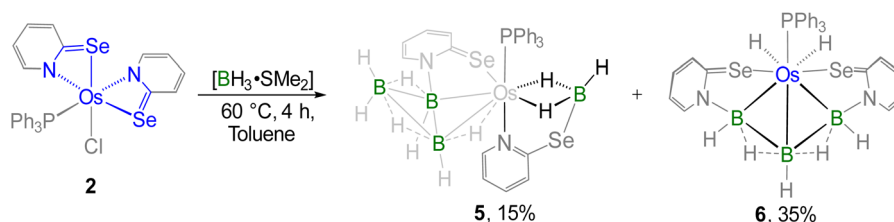


Fig. 4 Molecular structure and labelling diagram of **5**. Selected bond lengths (Å) of **5**: Os1-B1 2.223(8), Os1-B2 2.306(8), Os1-B4 2.056(8), Os1-N2 2.132(5); B1-B2 1.758(12), B2-B3 1.771(13), B3-B1 1.862(12), and Se2-B4 2.001(8) (aromatic hydrogens are not shown for better clarity).

resonances at $\delta = -0.39$ and -2.64 ppm emerged, which can be attributed to two distinct B-H-B units. These findings indicate rapid exchange between the B-H-B and terminal B-H protons at room temperature. Note that a similar dynamic behaviour has also been reported for rhodotetraborane dihydride, $[Rh(\eta^2-B_3H_8)(H)_2(PPh_3)_2]$.^{24a}

On the other hand, the remaining coordination sites in complex **5** were occupied by one PPh_3 ligand and a chelating ligand, $[H_3BL]^-$ in a κ^3-H,H,N bonding mode, leading to the formation of an Os-dihydridoborate moiety. The formation of this Os-dihydridoborate entity is proposed to result from the insertion of BH_3 into the Os-Se bond of the κ^2-N,Se -chelated ring in complex **5**. The Os1-B4 separation aligns well with that observed in the Os-dihydridoborate complex, $[Os(PPh_3)(\kappa^2-N,S-C_5H_4NS)\{\kappa^3-H,H,S-H_3BO(C_5H_4NS)\}]$,^{17c} but it is significantly shorter than the bond lengths typically found in TM-(σ -borane/borate) species.^{25,26} The bond separations of B4-Se2 and C12-Se2 are consistent with the typical ranges for B-Se and C-Se single bonds, respectively.²⁷ Thus, complex **5** can be designated as an Os(dihydridoborate)(octatrihydridoborate) species, with the formulation $[Os(PPh_3)(\kappa^3-H,H,N-BH_3L)\{\kappa^2-H,Se-B_3H_7L\}]$. The formation of **5** likely proceeds *via* two concurrent steps: (i)



Scheme 2 Cooperative borane activation utilizing Os(III)-N,Se-chelated complex **2**.

the insertion of a preformed triborane fragment into the Os–N bond, resulting in the formation of the Os–octahydridotriborate unit, and (ii) the cooperative activation of two B–H bonds from BH₃ through the cleavage of the Os–Se bond in another hemilabile OsNCSe metallacycle, which eventually furnishes the Os(dihydridoborate) unit. It is worth noting that this process constitutes a rare example of cooperative activation of borane in which both types of M–E bonds (E = N, Se) in hemilabile metallaheterocycle undergo cleavage.

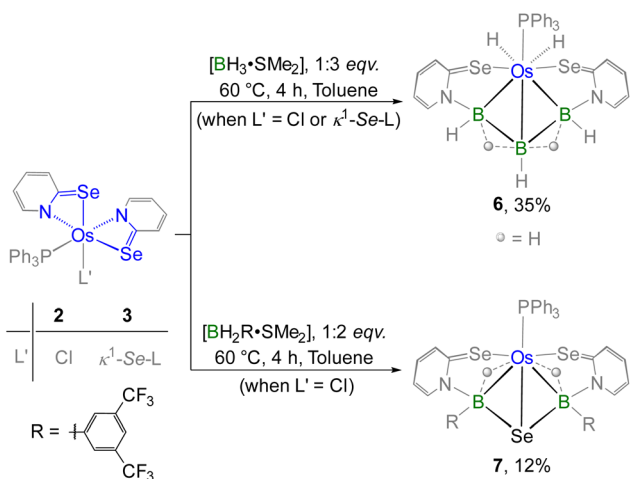
Furthermore, complex **6** was obtained as a yellow crystalline solid after chromatographic separation. Notably, **6** could also be isolated in improved yield when [BH₃·SMe₂] was treated with the non-innocent ligand based Os–N,Se-chelated complex, **3** (Scheme 3). The ¹¹B{¹H} NMR spectrum of **6** displayed two distinct resonance signals at δ = 17.0 and –39.0 ppm, indicating the existence of two different boron environments. Furthermore, single phosphorus and selenium environments were identified by the singlet resonance at δ = 16.1 ppm in the ³¹P{¹H} NMR spectrum and at δ = 234.8 ppm in the ⁷⁷Se NMR spectrum, respectively. In the upfield region of the ¹H NMR spectrum of **6**, two non-equivalent hydride signals were detected at δ = –13.40 and –1.41 ppm, which presumably arise due to the presence of M–H and B–H–B protons, respectively. The ESI-MS data of **6** exhibited an isotopic pattern at *m/z* 805.0319 that aligns with the molecular formula [C₂₈H₁₅PN₂Se₂B₃Os]. Although spectroscopic data in combination with mass spectrometry indicated the formation of an osmium borallyl species, structural confirmation was obtained by X-ray diffraction analysis of **6**. The molecular structure of **6** reveals an Os–borallyl complex characterized by a primary η³-borallyl coordination of the [B₃H₅L₂]^{2–} fragment, along with secondary interactions involving the selenopyridinyl selenium atom (Fig. S1). The spectroscopic and structural characteristics of **6** are consistent with those of a recently reported Os–borallyl complex, [(PPh₃)(H)₂Os(η⁵-B₃H₅(C₅H₄NS)₂)].²⁸ Similar to the analogous complex, the presence of two hydride ligands in **6** was confirmed by the sharp upfield resonance signal at δ =

–13.40 ppm in the ¹H NMR spectrum. The formation of **6** can be attributed to the insertion of the triborane unit facilitated by the ring opening of two osma-heterocycles.

As part of our ongoing research, we have studied the unconventional dual-site activation of both free and bulky boranes by the redox-active species, VI^{Ru}. (*vide supra*, Chart 1).^{17b} Strikingly, the activation of free boranes led to the formation of [Ru(PPh₃){κ³-H,S,S'-(NH₂BSBH₂N)(S₂C₇H₄)₂}], while a unique Ru-bis(dihydridoborate) complex was obtained from the cooperative activation of BH₂Mes (Mes = (CH₃)₃C₆H₃).^{17b} To investigate the influence of steric and electronic characteristics of substituted aryl groups of boranes on the cooperative activation process, we carried out reactions of complexes **2** and **3** with [BH₂R·SMe₂] and [BHR₂·SMe₂] (R = (CF₃)₂C₆H₃) (Scheme 3). Thermolysis of **2** with two equivalents of [BH₂R·SMe₂] generated **7** in 12% yield along with a few air-sensitive products, whereas complex **3** underwent decomposition under the same reaction conditions. The ³¹P{¹H} NMR spectrum of **7** revealed a sharp singlet at δ = 22.3 ppm which suggested the retention of the PPh₃ group. Similar to the ³¹P{¹H} NMR spectrum, a single resonance was observed at δ = 27.8 ppm in the ¹¹B{¹H} NMR spectrum and at δ = –62.2 ppm in the ¹⁹F{¹H} NMR spectrum. This suggested the presence of a highly symmetric geometry with chemically equivalent phosphorus, boron, and fluorine environments. Furthermore, the ¹H NMR spectrum of **7** showed a broad upfield resonance at δ = –9.72 ppm, likely arising from the presence of an Os–H–B unit. Notably, no characteristic broad resonance corresponding to a terminal B–H proton was observed in the ¹H NMR spectrum. However, the precise structure of **7** remained unresolved until solid-state X-ray diffraction analysis was performed on orange, needle-like crystals grown from a CH₂Cl₂ : hexane mixture at –5 °C.

As depicted in Fig. 5, complex **7** adopts a symmetrical core geometry featuring a mirror plane passing through the Se3–Os1–P1 fragment, which allows us to classify the molecule under C_s point group. The molecular structure of **7** consists of two five-membered {OsBNCSe} osmacycles fused *via* a single {OsB₂Se} butterfly unit, where osmium and selenium were positioned at the hinge tips and boron atoms were located at the wing tips. Although we were unable to find any proper mechanistic evidence, we believe that the Se atom in the butterfly core is presumably generated from the C–Se bond cleavage of the selenopyridinyl moiety. Interestingly, complex **7** can be viewed as a tetraborane derivative, exhibiting structural and electronic resemblance with the Os–borallyl species, **6** and [(PPh₃)(H)₂Os(η⁵-B₃H₅(C₅H₄NS)₂)].²⁸ The average Os–B distance (2.263 Å) is elongated in comparison to the average Ru–B bond length of the analogous species, [(PPh₃)Ru{κ³-H,S,S'-(NH₂BSBH₂N)(S₂C₇H₄)₂}],^{17b} yet it aligns well with the typical distances observed in osmium-based σ-borane/borate species.²⁹ Moreover, the average B–Se distance of 2.103 Å is slightly higher than that found in typical borane–selenate species.²⁷ The formation of **7** can be described by the insertion of two BHR units *via* ring opening of both the Os–N bonds and subsequent formation of B–Se bonds.

TM–borallyl complexes and their analogues are often unreactive due to the strong bonding between the borallyl entity



Scheme 3 Cooperative activation of free and substituted boranes utilizing paramagnetic Os(III)–N,Se-chelated species, **2**–**3**.



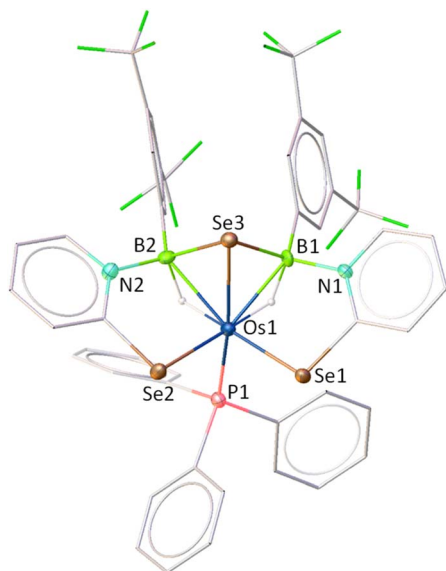
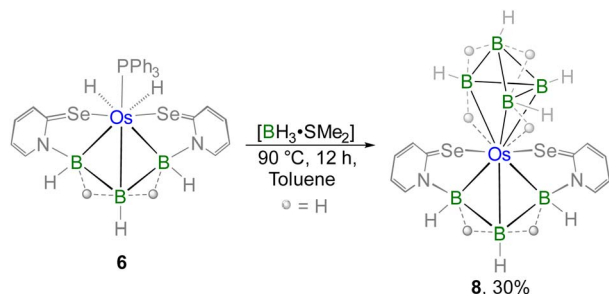


Fig. 5 Molecular structure and labelling diagram of **7**. Selected bond lengths (Å) and bond angles (°) of **7**: Os1–Se1 2.4771(7), Os1–Se2 2.4705(7), Os1–Se3 2.5612(7), Os1–B1 2.289(7), Os1–B2 2.237(7), B1–Se3 2.113(7); B2–Se3 2.093(7) (aromatic hydrogens are not shown for better clarity).

and the metal centre. Additionally, these complexes typically feature strongly π -acidic or π -basic ligands, which further restrict their reactivity.^{28,30} However, in the case of complex **6**, the osmium centre is coordinated to two hydride ligands and one PPh₃ ligand which are relatively labile. To examine their lability, we performed prolonged thermolysis of **6** with an excess of [BH₃·SMe₂] that yielded complex **8** in moderate yield (Scheme 4). The ³¹P {¹H} NMR analysis of **8** revealed no resonance peaks, indicating the loss of the PPh₃ unit from **6**. The ¹H NMR spectrum of **8** at room temperature displayed broad resonance signals in the upfield region at $\delta = -9.83, -4.19, -2.79, -1.44, -1.29$ and -0.54 ppm. These broad signals are due to the presence of either M–H–B or B–H–B protons. Additionally, in the ¹H NMR spectrum, multiple sets of broad signals were observed in the range of $\delta = 3.74$ – 2.66 ppm that correspond to terminal B–H protons while the ¹¹B{¹H} NMR spectrum shows peaks at $\delta = 12.2, 10.4, 8.9, -2.6, -7.2, -10.3, -11.5, -21.3, -22.4,$ and -28.1 ppm. The mass spectrometric



Scheme 4 Pyrolysis of Os-borallyl species [(PPh₃)(H)₂Os(η^5 -B₃H₅(-C₅H₄NSe₂))], **6** with excess borane.

data revealed an isotopic distribution pattern at m/z 593.0291. The comprehensive spectroscopic analysis suggests a highly asymmetrical nature of the complex. However, a definitive structure could not be established until X-ray diffraction analysis was conducted.

The X-ray diffraction study was carried out on a suitable yellow crystal obtained from the slow evaporation of a 9/1 DCM/hexane solution of **8** at -4 °C. The solid-state X-ray diffraction study of **8** revealed an unusual geometry surrounding the osmium centre (Fig. 6). One part of the structure can be described as an Os-borallyl entity, wherein the triborane ligand [B₃H₅(C₅H₄NSe₂)]²⁻ coordinates to the osmium centre in an η^3 -fashion. The other part of the molecule resembles a pentaborane derivative, where the osmium atom occupies one of the vertices in the basal plane of a square pyramidal geometry. The core geometry of **8** can be best described as a fusion of a butterfly {OsB₃} unit with a square pyramidal {OsB₄} unit, with the osmium centre serving as the common vertex. The B–B and Os–B bond lengths in **8** fall within the range reported for metallaborane clusters.^{31,32} Notably, the average B–B bond length in the tetraborane analogue (1.83 Å) is slightly longer as compared to that of the pentaborane analogue (1.73 Å). However, the Os–B bond lengths in the osmatetraborane unit are comparatively longer than those in the osmatriborane unit. The formation of **8** probably proceeds *via* a two-step pathway: initial dissociation of PPh₃ from complex **6**, followed by the formation of {OsB₄H₈} *via* monoborane pyrolysis.^{32,33} Notably, a careful assessment of the crystallographic data revealed the presence of two different isomeric forms of **8** (Fig. S2 and S3). The primary distinction between these isomers lies in the relative orientation of the square-pyramidal {OsB₄} unit with respect to the butterfly {OsB₃} one. The co-existence of these isomers in solution accounts for the complexity observed in the ¹H and ¹¹B NMR spectra (Fig. S36–S40). Similar instances of isomeric co-existence have also been well observed in TM-complexes and metallaborane clusters.³⁴

Notably, both complexes **6** and **8** feature a borallyl entity stabilized by heterocyclic ligand assisted secondary interactions involving the selenopyridinyl selenium atom. However, the

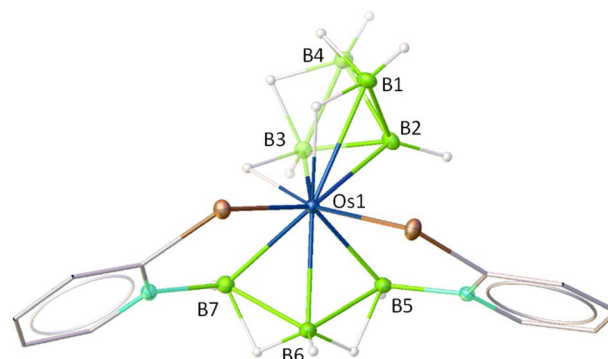


Fig. 6 Molecular structure and labelling diagram of **8**. Selected bond lengths (Å) of **8**: Os1–B1 2.416(3), Os1–B2 2.210(3), Os1–B3 2.268(3), B1–B2 1.713(4), and B1–B4 1.788(4) (aromatic hydrogens are not shown for better clarity).



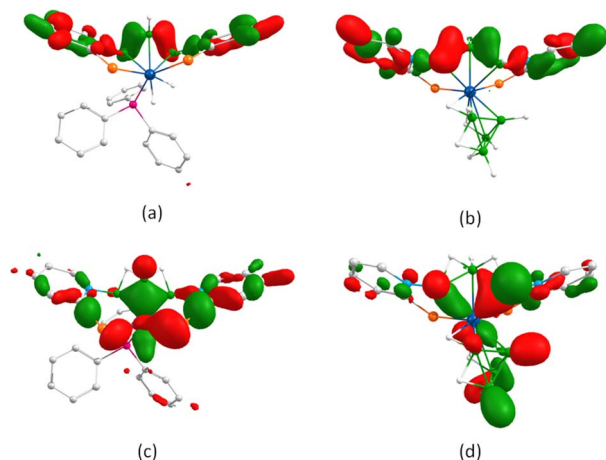
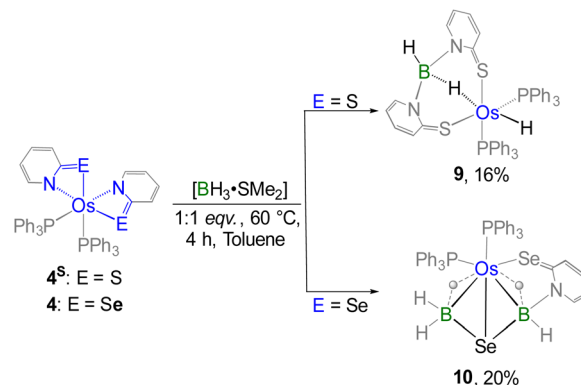


Fig. 7 (a) HOMO–37 of **6** (b) HOMO–26 of **8**; (c) HOMO–27 of **6**; (d) HOMO–14 of **8** (isovalue 0.004 [e per bohr³]^{1/2}).

bonding characteristics of other counterparts differ significantly from each other. To understand how this variation influences the bonding mode of the borallyl entity, we conducted DFT calculations. Molecular orbital (MO) analysis revealed that HOMO–37 of **6** exhibits extended bonding interaction across the triborane fragment (Fig. 7(a)), similar to the related complex [(PPh₃)(H)₂Os(η⁵-B₃H₅(C₅H₄NS)₂)]₂.²⁸ Similarly, HOMO–26 of **8** displays a comparable interaction but with enhanced energy stabilization (Fig. 7(b)). The bonding interaction between osmium and the triborane unit is particularly pronounced in HOMO–27 of **6** (Fig. 7(c)) and HOMO–14 of **8** (Fig. 7(d)), with greater stabilization observed in the case of **6**. This highlights the increased stability of the osmium borallyl framework in the presence of the PPh₃ counterpart. This observation is also consistent with the lower charge accumulation on the wing-tip boron atoms of the borallyl unit in species **6**. Moreover, HOMO–21 and HOMO–25 of **8** indicate the presence of substantial multi-centred bonding interactions within the {OsB₄} square pyramidal core.

Furthermore, we shifted our attention to the diamagnetic bis-κ²-*N*,*Se*-chelated species **4**, which is analogous to recently reported [Os(PPh₃)₂(κ²-*N*,*S*-C₅H₄NS)₂], **4**^S.^{17c} Notably, complex **4**^S undergoes cooperative borane activation, where two inequivalent B–H activation events led to the formation of an Os(σ-borate)hydride species, **9** (Scheme 5).^{17c} The primary difference between complexes **4** and **4**^S lies in the identity of their chalcogen atoms. Additionally, complex **4** is distinct from complexes **2** and **3** due to the different oxidation state of the osmium centre. To evaluate the impact of these electronic factors on metal–ligand cooperativity (MLC), complex **4** was subjected to the cooperative activation of both free and substituted borane. Treatment of **4** with one equivalent of [BH₃·SMe₂] led to the formation of complex **10** (Scheme 5). Interestingly, the ¹¹B NMR spectrum of **10** displayed two signals at δ = 0.6 and –21.0 ppm, indicating the presence of two inequivalent boron environments. Likewise, the upfield region of the ¹H NMR spectrum exhibited two broad signals at δ = –14.14 and –11.17 ppm, corresponding to two distinct Os–H–B



Scheme 5 Cooperative activation of free borane utilizing diamagnetic Os(II)-*N*,*E*-chelated complexes (E = S, Se).

units. Following the reaction, the appearance of two well-separated ³¹P{¹H} NMR signals implied the emergence of an asymmetric phosphorus environment. Nonetheless, a detailed interpretation remained elusive until single-crystal X-ray diffraction analysis of complex **10** was conducted.

As depicted in Fig. 8, the molecular structure of complex **10** reveals an octahedral geometry around the osmium centre, in which two PPh₃ ligands, two bridging hydride ligands, and two selenium atoms are each positioned *cis* to one another. Similar to complex **7**, complex **10** also contains a butterfly-shaped {OsB₂Se} core and can thus be classified as a tetraborane derivative. The dihedral angle across the butterfly-shaped core in complex **10** (103.8°) is considerably smaller than that observed in the analogous complex **7** (112.2°) and the Os–borallyl species **6** (111.7°). This difference may be attributed to the presence of two inequivalent tetracoordinate borate moieties in complex **10**, wherein one of the boron centres (B2) lacks coordination to a selenopyridinyl unit. Furthermore, the Os–Se and average B–Se bond distances are comparable in both complexes **7** and **10**. Notably, the average Os–B bond length in complex **10** (2.376 Å) is significantly longer than that in complex **7** (2.263 Å),

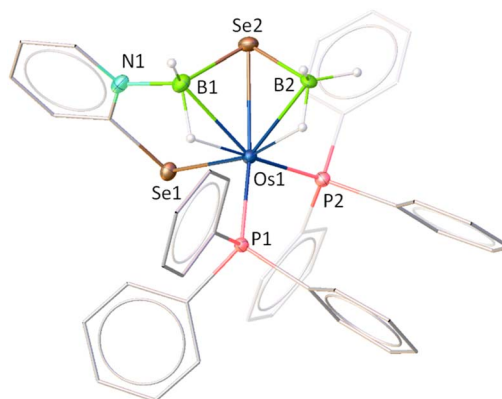


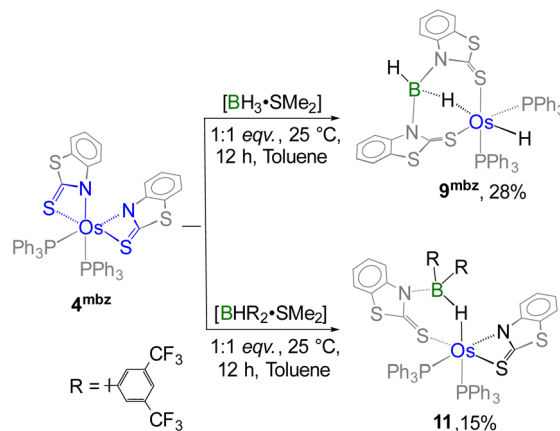
Fig. 8 Molecular structure and labelling diagram of **10**. Selected bond lengths (Å) of **10**: Os1–Se1 2.4950(5), Os1–Se2 2.529(2), Os1–B1 2.375(6), Os1–B2 2.380(5), B1–Se2 2.053(7); B2–Se2 2.078(6) (aromatic hydrogens and carbons are not shown for better clarity).



likely due to the presence of electron-withdrawing substituents in complex **7**.

The presence of the {OsB₂Se} butterfly core with distinct ligand environments in both **7** and **10** prompted us to explore their bonding scenario. Molecular orbital (MO) analysis demonstrates that the HOMOs in both complexes are predominantly localized on the osmium centre and the selenium atom within the selenopyridinyl ring, whereas the LUMOs exhibit π -orbital delocalization across the pyridinyl ring. Importantly, the HOMO–LUMO energy gaps ($\Delta E_{\text{HOMO-LUMO}}$) are nearly identical for both complexes. Similarly, variations in ligand environments do not significantly influence the interaction between the osmium atom and the free selenium atom, as reflected by their similar bond distances and Wiberg bond index (WBI) values (Table S2). Natural bonding orbital (NBO) analysis further revealed the presence of three-centre two-electron (3c–2e) bonding interactions along the Os–H–B moieties (Fig. 9). In complex **7**, the two boron atoms exhibit comparable natural charges, whereas in complex **10**, the B1 atom shows higher charge accumulation than B2. This suggests that B1 possesses a more pronounced borate character, likely due to differences in its electronic environment.

On the other hand, complex **4** underwent decomposition when reacted with substituted boranes, [BH₂R·SMe₂] and [BHR₂·SMe₂]. To facilitate the cooperative activation of bulkier aryl-substituted boranes, we employed an alternative diamagnetic bis- κ^2 -*N,S*-chelated species, [Os(PPh₃)₂(κ^2 -*N,S*-C₇H₄NS₂)₂] (**4**^{mbz}) in which the heterocyclic ligands impart a distinct electronic environment compared to its analogous species. Similar to the case of **4**^S, the cooperative B–H activation of free borane utilizing **4**^{mbz} resulted in the formation of the Os(σ -borate) hydride species, **9**^{mbz}.^{17c} Building on this finding, the reaction of **4**^{mbz} with one equivalent of [BHR₂·SMe₂] at room temperature



Scheme 6 Cooperative activation of free and substituted boranes utilizing diamagnetic Os(II)–*N,S*-chelated complex **4**^{mbz}.

afforded complex **11** (Scheme 6). In contrast, reaction with [BH₂R·SMe₂] generated air and moisture-sensitive products in low yield. Complex **11** was isolated in 15% yield after chromatographic separation and further characterized by multinuclear spectroscopy, mass spectrometry and solid-state X-ray diffraction. The ¹¹B{¹H} NMR spectrum revealed a resonance peak at $\delta = 2.2$ ppm that suggested the presence of a tetra-coordinated boron atom in a single environment. Furthermore, the ¹H NMR spectrum of **11** exhibited a broad signal in the shielded region at $\delta = -5.51$ ppm, which appeared relatively downfield compared to that in **10**. The observed chemical shift is presumably due to the electron-withdrawing effect of the aryl substituents attached to boron. Notably, the appearance of two separate sharp signals in the ³¹P{¹H} NMR spectrum implies that **4**^{mbz} experiences a reduction in symmetry following the reaction. Although the spectroscopic data suggested a probable activation of the B–H bond of BHR₂, a detailed understanding of the structural characteristics of **11** could only be obtained through solid-state X-ray diffraction analysis.

As shown in Fig. 10, complex **11** can be identified as a κ^2 -*N,S*-chelated Os(σ -borate) complex which can be formulated as [Os(PPh₃)₂(κ^2 -*N,S*-C₇H₄NS₂)₂](κ^3 -*H,S,S'*-HBR₂(C₇H₄NS₂)). The molecular structure of **11** exhibited a distorted octahedral geometry around the osmium centre with the retention of two PPh₃ units and one OsNCS metallacycle from **4**^{mbz}. Additionally, the formation of a nonplanar six-membered osma-heterocycle (OsHBNCs) can be attributed to the hemilabile ring opening of an Os–N bond, followed by the capture of a B–H bond of BHR₂. The Os–B separation in complex **11** is considerably larger than that found in reported Os(σ -borate) complexes²⁹ as well as other σ -borate complexes of group-8 TM.^{17,25a} It is noteworthy that one of the osma-heterocycles (OsNCS) remained intact after the reaction, and its bite angle is comparable to that of other OsNCS metallacycles.^{17c} However, we believe that the steric hindrance caused by the two aryl groups on the boron atom prevented the B–H activation of the second BHR₂ unit. Indeed, this can be considered as one of the rarest examples of cooperative activation involving a sterically demanding di-substituted borane.

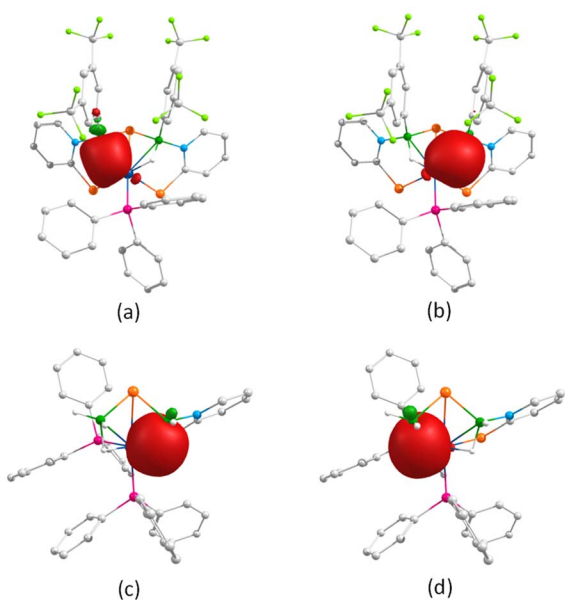


Fig. 9 3c–2e bonding interaction along the Os–H–B unit of **7** (a and b) and **10** (c and d) (isovalue 0.004 [e per bohr^{3/2}]).



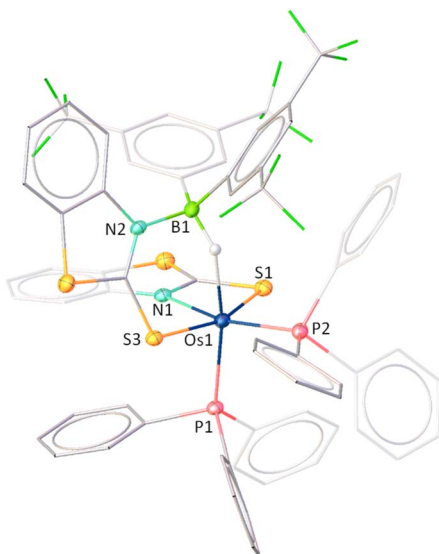


Fig. 10 Molecular structure and labelling diagram of **11**. Selected bond lengths (Å) and bond angles (°) of **11**: Os1–S1 2.441(3), Os1–S3 2.339(3), Os1–P1 2.309(3), Os1–P2 2.314(3), Os1–B1 3.001, and N1–Os1–S1 67.3(2) (aromatic hydrogens are not shown for better clarity).

DFT calculations offered valuable insights into the energetics of the cooperative B–H activation of BR_2H as well as the bonding nature in complex **11**. The observed negative Gibbs free energy change ($\Delta G = -12.6 \text{ kcal mol}^{-1}$) for this reaction indicates that the sterically hindered borane activation by **4**^{mbz} is thermodynamically favourable. Molecular orbital (MO) analysis revealed that HOMO is primarily localized on the metal centre and the mercaptobenzothiazolyl sulphur atoms, while the LUMO is mainly delocalized over the aryl substituents of boron with only marginal involvement of the metal centre. A notable HOMO–LUMO energy gap of 3.379 eV was identified for **11**. Natural bonding orbital (NBO) analysis further confirmed a strong donor–acceptor interaction between the $\sigma(\text{B–H})$ orbital and the Os centre in **11** (Fig. 11, left). Second-order perturbation theory estimated a substantial stabilization energy of 43.9 kcal mol⁻¹, emphasizing the strength of this interaction. Additionally, the σ -borate unit in **11** was found to exhibit bond critical points (BCPs) along the Os–H and B–H bonds (Fig. 11, right).

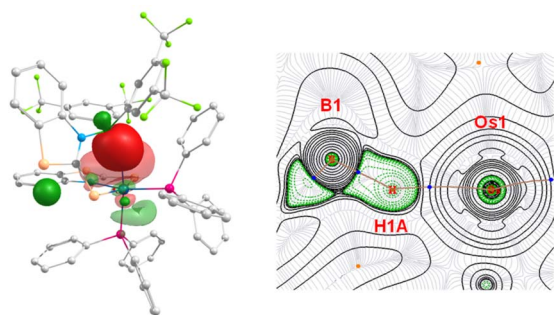


Fig. 11 Donor–acceptor interaction among the $\sigma(\text{B–H})$ orbital and Os centre in **11** (left); contour-line diagram of the Laplacian of the electron density along Os–H–B planes in **11** (right).

Conclusions

In this study, we have developed various Os(III)-based 1,3-*N,Se*-chelated complexes as model systems for investigating metal–ligand cooperativity. By systematically tuning the electronic characteristics of both the metal and the ligand frameworks, we modulated the hemilability of osma-heterocycle motifs. The modes of electron localization within these paramagnetic species were thoroughly characterized using spectroscopic, electrochemical, and photophysical techniques. To evaluate the impact of these tailored electronic characteristics, we investigated the cooperative activation of free borane. The cooperative activation of free borane employing the bis-1,3-*N,Se*-chelated Os(III) complex (**2**) resulted in the formation of a unique Os(dihydridoborate)(octatrihydridoborate) complex. This transformation proceeds *via* cleavage of both the Os–Se and Os–N bonds of two different metallacycles. In contrast, when employing complex **3**, the activation was dominated by selective Os–N bond cleavage, highlighting the sensitivity of the cooperative activation pathway to the electronic environment of the complex. We further examined the distinct activation pattern of sterically hindered boranes using various paramagnetic and diamagnetic bis-1,3-*N,E*-chelated complexes ($E = \text{S, Se}$). The mono- and di-substituted hydroboranes led to the formation of Os(σ -borate) species through cooperative B–H bond activation. Interestingly, with a sterically demanding di-aryl substituted borane, only one metallacycle unit underwent activation, while the second osma-heterocycle remained intact, presumably due to steric hindrance of aryl substituents. This study provides valuable insights into metal–ligand cooperativity and opens the way for the development of unique transition metal–boron complexes with potential applications in catalysis.

Author contributions

F. Assanar and S. Gayen have executed the experimental synthesis, characterization and analysis of the data. S. Gayen has performed the theoretical calculations. D. K. Patel has performed the X-ray diffraction analysis. All authors have contributed to the preparation of the manuscript. S. Ghosh and T. Pradeep have supervised the project.

Conflicts of interest

There are no conflicts to declare.

Data availability

The data supporting this article have been included as part of the supplementary information (SI). Supplementary information is available. See DOI: <https://doi.org/10.1039/d5sc06346a>.

CCDC 2481059 (**1**), 2481057 (**2**), 2466501 (**4**), 2481058 (**5**), 2466499 (**6**), 2466503 (**7**), 2466500 (**8**), 2472949 (**10**) and 2472945 (**11**) contain the supplementary crystallographic data for this paper.^{35a–i}



Acknowledgements

S. Ghosh acknowledges the support of the SERB, India, Grant No. CRG/2023/000189. T. Pradeep thanks SERB for funding through Grant No. SPR/2021/000439 and the JC Bose Fellowship. We thankfully acknowledge the support from the CoE on Molecular Materials and Functions under the IoE scheme, IIT Madras for the single crystal XRD facility. F. A. thanks UGC, S. G. thanks CSIR and D. K. P. thanks PMRF (Grant No. SB22230356CYPMRFF008224) for research fellowships. The computational facility of IIT Madras is gratefully acknowledged.

Notes and references

- (a) R. Peters, *Cooperative Catalysis*, Wiley-VCH, Weinheim, 2015; (b) J. Khusnutdinova and D. Milstein, *Angew. Chem., Int. Ed.*, 2015, **54**, 12236; (c) L. Buchwald and D. Milstein, *Ligand Design in Metal Chemistry: Reactivity and Catalysis*, John Wiley & Sons, 2016.
- (a) S. Schneider, J. Meiners and B. Askevold, *Eur. J. Inorg. Chem.*, 2012, 412–429; (b) B. Chatterjee, W. C. Chang, S. Jena and C. Werle, *ACS Catal.*, 2020, **10**(23), 14024–14055; (c) V. K. K. Praneeth, M. R. Ringenberg and T. R. Ward, *Angew. Chem., Int. Ed.*, 2012, **51**, 10228–10234.
- (a) O. R. Luca and R. H. Crabtree, *Chem. Soc. Rev.*, 2013, **42**, 1440–1459; (b) J. I. van der Vlugt and J. N. H. Reek, *Angew. Chem., Int. Ed.*, 2009, **48**, 8832–8846; (c) M. Stradiotto and R. J. Lundgren, *Ligand Design in Metal Chemistry*, Wiley Online Library, 2016.
- (a) M. Bassetti, *Eur. J. Inorg. Chem.*, 2006, 4473–4482; (b) P. O. Lagaditis, P. E. Sues, J. F. Sonnenberg, K. Y. Wan, A. J. Lough and R. H. Morris, *J. Am. Chem. Soc.*, 2014, **136**(4), 1367–1380; (c) F. Forster and M. Oestreich, *Metal–Ligand Cooperative Si–H Bond Activation in Organosilicon Chemistry—Novel Approaches and Reactions*, ed. T. Hiyama and M. Oestreich, Wiley-VCH, Weinheim, 2019, pp. 115–130; (d) L. Omann, C. D. F. Konigs, H. F. T. Klare and M. Oestreich, *Acc. Chem. Res.*, 2017, **50**(5), 1258–1269; (e) S. P. Cronin, J. M. Strain, M. S. Mashuta, J. M. Spurgeon, R. M. Buchanan and C. A. Grapperhaus, *Inorg. Chem.*, 2020, **59**(7), 4835–4841.
- (a) K.-S. Feichtner and V. H. Gessner, *Chem. Commun.*, 2018, **54**, 6540–6553; (b) C. C. Comanescu and V. M. Iluc, *Chem. Commun.*, 2016, **52**, 9048–9051; (c) Q. Liang, H. A. G. Mayerstein and D. Song, *Organometallics*, 2023, **42**(9), 816–824; (d) T. Higashi, S. Kusumoto and K. Nozaki, *Chem. Rev.*, 2019, **119**(8), 10393–10402; (e) S. Zhang, X. Zhai, Y. Song, L. Feng, C. H. Tung and W. Wang, *Organometallics*, 2021, **40**(11), 1692–1698; (f) M. G. Cameo, A. Urriolabeitia, E. Barrenas, V. Passarelli, J. J. Pérez-Torrente, A. D. Giuseppe, V. Polo and R. Castarlenas, *ACS Catal.*, 2021, **11**(12), 7553–7567; (g) B. Español-Sánchez, J. Moradell, M. Galiana-Cameo, E. Barrenas, J. J. Pérez-Torrente, V. Passarelli and R. Castarlenas, *Angew. Chem., Int. Ed.*, 2025, **64**, e202507424.
- (a) G. R. Owen, *Chem. Soc. Rev.*, 2012, **41**, 3535–3546; (b) G. Bouhadir and D. Bourissou, *Chem. Soc. Rev.*, 2016, **45**, 1065–1079; (c) J. A. Zurakowski, B. Stadler, M. W. Drover and M. R. Crimmin, *Angew. Chem., Int. Ed.*, 2025, **64**, e202512684.
- (a) W. H. Harman and J. C. Peters, *J. Am. Chem. Soc.*, 2012, **134**(11), 5080–5082; (b) A. M. Poitras, S. E. Knight, M. W. Bezpalko, B. M. Foxman and C. M. Thomas, *Angew. Chem., Int. Ed.*, 2018, **57**(6), 1497–1500; (c) W. H. Harman, T. P. Lin and J. C. Peters, *Angew. Chem., Int. Ed.*, 2014, **53**(4), 1081–1086.
- (a) C. Gunanathan and D. Milstein, *Acc. Chem. Res.*, 2011, **44**(8), 588–602; (b) R. H. Morris, *Acc. Chem. Res.*, 2015, **48**(5), 1494–1502; (c) M. Rauch, S. Kar, A. Kumar, L. Avram, L. J. W. Shimon and D. Milstein, *J. Am. Chem. Soc.*, 2020, **142**(34), 14513–14521; (d) Y. Liang, J. Luo, Y. D. Posner and D. Milstein, *J. Am. Chem. Soc.*, 2023, **145**(16), 9164–9175.
- (a) H. Li, M. Fan and Q. Liu, *J. Am. Chem. Soc.*, 2024, **146**(39), 26649–26656; (b) J. J. Gair, Y. Qiu, R. L. Khade, N. H. Chan, A. S. Filatov, Y. Zhang and J. C. Lewis, *Organometallics*, 2019, **38**(7), 1407–1412; (c) H. Li, T. P. Goncalves, D. Lupp and K. W. Huang, *ACS Catal.*, 2019, **9**(3), 1619–1629.
- (a) V. Lyaskovskyy and B. d. Bruin, *ACS Catal.*, 2012, **2**(2), 270–279; (b) D. L. Broere, R. Plessius and J. I. V. Vlugt, *Chem. Soc. Rev.*, 2015, **44**, 6886–6915; (c) O. R. Luca and R. H. Crabtree, *Chem. Soc. Rev.*, 2013, **42**, 1440–1459.
- (a) C. Erken, A. Kaithal, S. Sen, T. Weyhermuller, M. Holscher, C. Werle and W. Leitner, *Nat. Commun.*, 2018, **9**, 4521; (b) B. Wang, C. Rong, M. Lei, S. Liu and F. D. Proft, *Inorg. Chem.*, 2023, **62**(19), 7366–7375; (c) H. Song, K. Ye, P. Geng, X. Han, R. Liao, C.-H. Tung and W. Wang, *ACS Catal.*, 2017, **7**(11), 7709–7717; (d) M. Pang, C. Wu, X. Zhuang, F. Zhang, M. Su, Q. Tong, C.-H. Tung and W. Wang, *Organometallics*, 2018, **37**(9), 1462–1467; (e) X. Zhai, M. Pang, L. Feng, J. Jia, C. H. Tung and W. Wang, *Chem. Sci.*, 2021, **12**, 2885–2889.
- (a) M. R. Elsbey and R. T. Baker, *Chem. Commun.*, 2019, **55**, 13574–13577; (b) M. A. Nesbit, D. L. Sues and J. C. Peters, *Organometallics*, 2015, **34**(19), 4741–4752; (c) S. N. MacMillan, W. H. Harman and J. C. Peters, *Chem. Sci.*, 2014, **5**, 590–597; (d) S. Lau, D. Gasperini and R. L. Webster, *Angew. Chem., Int. Ed.*, 2021, **60**, 14272–14294; (e) L. A. Grose and D. Willcox, *Chem. Commun.*, 2023, **59**, 7427–7430.
- (a) J. F. C. Perez, F. L. Kirilin, E. F. Reynolds, C. E. A. Jarczyk, B. T. Joseph, J. M. Keith and A. R. Chianese, *ACS Catal.*, 2024, **14**(21), 16497–16507; (b) P. O. Lagaditis, P. E. Sues, J. F. Sonnenberg, K. Y. Wan, A. J. Lough and R. H. Morris, *J. Am. Chem. Soc.*, 2014, **136**(4), 1367–1380; (c) S. Werkmeister, K. Junge, B. Wendt, E. Alberico, H. Jiao, W. Baumann, H. Junge, F. Gallou and M. Beller, *Angew. Chem., Int. Ed.*, 2014, **53**(33), 8722–8726; (d) B. L. Ramirez and C. C. Lu, *J. Am. Chem. Soc.*, 2020, **142**, 5396–5407; (e) M. Hasenbeck, T. Müller and U. Gellrich, *Catal. Sci. Technol.*, 2019, **9**, 2438–2444.
- (a) K. Fujita, N. Tanino and R. Yamaguchi, *Org. Lett.*, 2007, **9**(1), 109–111; (b) A. M. Royer, T. B. Rauchfuss and D. L. Gray, *Organometallics*, 2010, **29**, 6763–6768.
- (a) M. W. Drover, L. L. Schafer and J. A. Love, *Angew. Chem., Int. Ed.*, 2016, **55**(9), 3181–3186; (b) M. W. Drover, J. A. Love



- and L. L. Schafer, *J. Am. Chem. Soc.*, 2016, **138**(27), 8396–8399; (c) N. M. Leeb, M. W. Drover, J. A. Love and L. L. Schafer, *Organometallics*, 2018, **37**(24), 4630–4638.
- 16 J. B. Geri and N. K. Szymczak, *J. Am. Chem. Soc.*, 2015, **137**(40), 12808–12814.
- 17 (a) Md. Zafar, R. Ramalakshmi, A. Ahmad, P. K. S. Antharjanam, S. Bontemps, S. S. Etienne and S. Ghosh, *Inorg. Chem.*, 2021, **60**(2), 1183–1194; (b) M. Zafar, A. Ahmad, S. Saha, R. Rongala, T. Roisnel and S. Ghosh, *Chem. Sci.*, 2022, **13**, 8567–8575; (c) S. Gayen, F. Assanar, S. Shyamal, D. P. Dorairaj and S. Ghosh, *Chem. Sci.*, 2024, **15**, 15913–15924.
- 18 (a) M. Zafar, R. Ramalakshmi, K. Pathak, A. Ahmad, T. Roisnel and S. Ghosh, *Chem. Eur J.*, 2019, **25**, 13537–13546; (b) A. Ahmad, S. Saha, M. Zafar, T. Roisnel, P. Ghosh and S. Ghosh, *Eur. J. Org. Chem.*, 2023, **989**, e202201283.
- 19 (a) S. Saha, A. Haridas, F. Assanar, C. Bansal, P. K. S. Antharjanam and S. Ghosh, *Dalton Trans.*, 2022, **51**, 4806–4813; (b) S. Saha, F. Assanar, A. Ahmad, A. Bains, S. Nagendran and S. Ghosh, *Organometallics*, 2024, **43**(7), 718–725.
- 20 (a) R. E. DeSimone, *J. Am. Chem. Soc.*, 1973, **95**(19), 6238–6244; (b) P. Singh, B. Sarkar, M. Sieger, M. Niemeyer, J. Fiedler, S. Zalis and W. Kaim, *Inorg. Chem.*, 2006, **45**(12), 4602–4609.
- 21 (a) P.-S. Kuhn, G. E. Buchel, K. K. Jovanovic, L. Filipovic, S. Radulovic, P. Rapta and V. B. Arion, *Inorg. Chem.*, 2014, **53**, 11130–11139; (b) F. Chen, G.-F. Wang, Y.-Z. Li, X.-T. Chen and Z.-L. Xue, *Inorg. Chem. Commun.*, 2012, **21**, 88–91.
- 22 K. W. Given, S. H. Wheeler, B. S. Jick, L. J. Maheu and L. H. Pignolet, *Inorg. Chem.*, 1979, **18**, 1261–1266.
- 23 (a) N. N. Greenwood, J. D. Kennedy, M. T. Pett and J. D. Woollins, *J. Chem. Soc., Dalton Trans.*, 1985, 2397–2406; (b) M. Bown, X. L. R. Fontaine, N. N. Greenwood, P. MacKinnon, J. D. Kennedy and M. T. Pett, *J. Chem. Soc., Dalton Trans.*, 1987, 2781–2787.
- 24 (a) F. Diaw-Ndiaye, P. J. S. Miguel, R. Rodríguez and R. Macías, *Molecules*, 2023, **28**(18), 6462; (b) A. Ahmad, S. Saha, M. Zafar, M. Cordier and S. Ghosh, *Eur. J. Inorg. Chem.*, 2023, **26**, e202300196.
- 25 (a) K. Saha, D. K. Roy, R. D. Dewhurst, S. Ghosh and H. Braunschweig, *Acc. Chem. Res.*, 2021, **54**, 1260–1273; (b) K. Saha, R. Ramalakshmi, S. Gomosta, K. Pathak, V. Dorcet, T. Roisnel, J.-F. Halet and S. Ghosh, *Chem. Eur J.*, 2017, **23**, 9812–9820; (c) S. Gayen, S. Shyamal, S. Mohapatra, P. K. S. Antharjanam and S. Ghosh, *Chem. Eur J.*, 2024, **30**, e202302362; (d) M. R. St.-J. Foreman, A. F. Hill, G. R. Owen, A. J. P. White and D. J. Williams, *Organometallics*, 2003, **22**, 4446–4450.
- 26 (a) C. Lenczyk, D. K. Roy, J. Nitsch, K. Radacki, F. Rauch, R. D. Dewhurst, F. M. Bickelhaupt, T. B. Marder and H. Braunschweig, *Chem. Eur J.*, 2019, **25**, 13566–13571; (b) R. N. Perutz, S. S. Etienne and A. S. Weller, *Angew. Chem., Int. Ed.*, 2021, **60**, 2–24; (c) C. N. Muhoro, X. He and J. F. Hartwig, *J. Am. Chem. Soc.*, 1999, **121**(21), 5033–5046.
- 27 (a) D. Auerhammer, M. Arrowsmith, R. D. Dewhurst, T. Kupfer, J. Bohnke and H. Braunschweig, *Chem. Sci.*, 2018, **9**, 2252–2260; (b) A. Ahmad, S. Gayen, S. Mishra, Z. Afsan, S. Bontemps and S. Ghosh, *Inorg. Chem.*, 2024, **63**(7), 3376–3382.
- 28 S. Gayen, S. Shyamal, F. Assanar and S. Ghosh, *Organometallics*, 2024, **43**(22), 2935–2943.
- 29 (a) M. L. Buil, J. J. F. Cardo, M. A. Esteruelas, I. Fernandez and E. Onate, *Organometallics*, 2015, **34**(3), 547–550; (b) J. C. Babon, M. A. Esteruelas, I. Fernandez, A. M. Lopez and E. Onate, *Inorg. Chem.*, 2018, **57**(8), 4482–4491; (c) N. Arnold, S. Mozo, U. Paul, U. Radius and H. Braunschweig, *Organometallics*, 2015, **34**(24), 5709–5715.
- 30 X. Lei, M. Shang and T. P. Fehlner, *Organometallics*, 1998, **17**(8), 1558–1563.
- 31 (a) S. Shyamal, D. Chatterjee, K. Kar and S. Ghosh, *Inorg. Chem.*, 2024, **63**(46), 21838–21848; (b) K. Kar, S. Kar and S. Ghosh, *Chem. Sci.*, 2024, **15**, 4179–4186.
- 32 (a) S. K. Bose, K. Geetharani, B. Varghese and S. Ghosh, *Inorg. Chem.*, 2010, **49**(14), 6375–6377; (b) K. Geetharani, B. S. Krishnamoorthy, S. Kahlal, S. M. Mobin, J.-F. Halet and S. Ghosh, *Inorg. Chem.*, 2012, **51**(19), 10176–10184; (c) R. Borthakur, K. Saha, S. Kar and S. Ghosh, *Coord. Chem. Rev.*, 2019, **399**, 213021; (d) S. Kar, A. N. Pradhan and S. Ghosh, *Coord. Chem. Rev.*, 2021, **436**, 213796.
- 33 (a) S. Ghosh, B. C. Noll and T. P. Fehlner, *Dalton Trans.*, 2008, 371–378; (b) S. Sahoo, R. S. Dhayal, B. Varghese and S. Ghosh, *Organometallics*, 2009, **28**(5), 1586–1589; (c) S. Ghosh, B. C. Noll and T. P. Fehlner, *Angew. Chem., Int. Ed.*, 2005, **44**(19), 2916–2918; (d) R. S. Anju, D. K. Roy, K. Geetharani, B. Mondal, B. Varghese and S. Ghosh, *Dalton Trans.*, 2013, **42**, 12828–12831.
- 34 (a) J. R. Shapley, J. T. Park, M. R. Churchill, C. Bueno and H. J. Wasserman, *J. Am. Chem. Soc.*, 1981, **103**, 7385–7387; (b) U. Kölle, J. Kossakowski, N. Klaff, L. Wesemann, U. Englert and G. E. Herberich, *Angew. Chem., Int. Ed.*, 1991, **30**, 690–691; (c) S. Ghosh, X. Lei, C. L. Cahill and T. P. Fehlner, *Angew. Chem., Int. Ed.*, 2000, **39**, 2900–2902.
- 35 (a) CCDC 2481059: Experimental Crystal Structure Determination, 2025, DOI: [10.5517/ccdc.csd.cc2p8r5x](https://doi.org/10.5517/ccdc.csd.cc2p8r5x); (b) CCDC 2481057: Experimental Crystal Structure Determination, 2025, DOI: [10.5517/ccdc.csd.cc2p8r3v](https://doi.org/10.5517/ccdc.csd.cc2p8r3v); (c) CCDC 2466501: Experimental Crystal Structure Determination, 2025, DOI: [10.5517/ccdc.csd.cc2nslkm](https://doi.org/10.5517/ccdc.csd.cc2nslkm); (d) CCDC 2481058: Experimental Crystal Structure Determination, 2025, DOI: [10.5517/ccdc.csd.cc2p8r4w](https://doi.org/10.5517/ccdc.csd.cc2p8r4w); (e) CCDC 2466499: Experimental Crystal Structure Determination, 2025, DOI: [10.5517/ccdc.csd.cc2nslhk](https://doi.org/10.5517/ccdc.csd.cc2nslhk); (f) CCDC 2466503: Experimental Crystal Structure Determination, 2025, DOI: [10.5517/ccdc.csd.cc2nslmp](https://doi.org/10.5517/ccdc.csd.cc2nslmp); (g) CCDC 2466500: Experimental Crystal Structure Determination, 2025, DOI: [10.5517/ccdc.csd.cc2nsljl](https://doi.org/10.5517/ccdc.csd.cc2nsljl); (h) CCDC 2472949: Experimental Crystal Structure Determination, 2025, DOI: [10.5517/ccdc.csd.cc2p09kl](https://doi.org/10.5517/ccdc.csd.cc2p09kl); (i) CCDC 2472945: Experimental Crystal Structure Determination, 2025, DOI: [10.5517/ccdc.csd.cc2p09fg](https://doi.org/10.5517/ccdc.csd.cc2p09fg).

